ELSEVIER

Contents lists available at ScienceDirect

# Sensors and Actuators A: Physical

journal homepage: www.elsevier.com/locate/sna



# Monitoring of random microvessel network formation by in-line sensing of flow rates: A numerical and *in vitro* investigation



Vladimir A. Pozdin<sup>a,b,1</sup>, Patrick D. Erb<sup>c,1</sup>, McKenna Downey<sup>d</sup>, Kristina R. Rivera<sup>c</sup>, Michael Daniele<sup>c,d,\*</sup>

- <sup>a</sup> Department of Electrical & Computer Engineering, Florida International University, 10555 West Flagler St., Miami, FL, 33174, USA
- b Department of Mechanical & Materials Engineering, Florida International University, 10555 West Flagler St., Miami, FL, 33174, USA
- <sup>c</sup> Joint Department of Biomedical Engineering, North Carolina State University and University of North Carolina at Chapel Hill 911 Oval Dr., Raleigh, NC, 27695. USA
- d Department of Electrical & Computer Engineering, North Carolina State University, 890 Oval Dr., Raleigh, NC, 27695, USA

# ARTICLE INFO

# Article history: Received 17 August 2020 Received in revised form 25 May 2021 Accepted 8 July 2021 Available online 10 July 2021

Keywords:
Microphysiological systems
Microfluidics
Equivalent circuit
Fluid mechanics
Vascular mechanics
Microvessels
Fluid networks

# ABSTRACT

The directed or de novo formation of microvasculature in engineered tissue constructs is essential for accurately replicating physiological function. A limiting factor of a system relying on spontaneous microvessel formation is the inability to precisely quantify the development of the microvascular network and control fluid moving through formed vessels. Herein, we report a strategy to monitor the dynamic formation of microscale fluid networks, which can be translated to the monitoring of microvasculature development in engineered tissue constructs. The non-invasive, non-destructive monitoring and characterization of the fluid network is achieved via in-line sensing of fluid flow rate and correlating this measurement to the hydrodynamic resistance of the fluid network to model the progression of microvessel formation and connectivity. Computational fluid dynamics, equivalent circuit, and experimental models were compared, which simulated multi-generational branching or splitting microvessel networks. The networks simulated vessels with varying cross-sectional area, up to 16 branching vessels, and microvessel network volume ranging from  $\tilde{2}0-30~\text{mm}^3$ . In all models, the increasing degree of network complexity and volume corresponded to a decrease in jumper flow-rate measured; however, vessel cross-section also impacted the measured jumper flow rate, i.e. at low vessel height (<200 µm) response was dominated by increased network volume and at higher vessel height (>200 µm) the response was dominated by resistance of narrow channels. An approximately 2% error was exhibited between the models, which was attributed to variation in the geometry of the fabricated models and illustrates the potential to precisely and non-destructively monitor microvessel network development and volumetric changes.

© 2021 Elsevier B.V. All rights reserved.

# 1. Introduction

Microphysiological systems (MPS) integrate 3D engineered tissue constructs onto microfluidic platforms to mimic the physicochemical function of human organs and tissues [1]. MPS fabricated from primary human cells can bridge the gap between cell culture and animal models, while informing clinical testing [2]. MPS also provide a precision platform to investigate specific physiological phenomena. In the past decade, multiple companies have

emerged with research-grade MPS for preliminary toxicological screening and pharmacokinetic studies, including liver (C.N. BioInnovations), lung (Emulate, Inc.), intestine (Altis Biosystems), and heart (Hesperos, Inc.) chip models [3]. As MPS advance to model more complex organ function for longitudinal developmental and drug discovery studies [4], there remain many challenges to overcome concerning MPS longevity in long-term studies and sacrificial endpoint analyses.

One major challenge for the advancement of MPS is the incorporation and real-time characterization of functional vascular networks [5]. Although continuous fluid flow through microchannels is a common feature of MPS, media most often travels as a wide fluid sheet across a semi-permeable barrier or monolayer of cells [6]. In the human body, vasculature is oriented as stochastic and

<sup>\*</sup> Corresponding author at: Department of Electrical & Computer Engineering, North Carolina State University, 911 Oval Dr., Raleigh, NC, 27695, USA.

E-mail address: mdaniel6@ncsu.edu (M. Daniele).

<sup>&</sup>lt;sup>1</sup> These authors contributed equally to this paper.

ad hoc networks of various microvessels with varied diameter and length, from the miniscule single cell <10 µm diameter capillaries to the huge cm-wide aorta and vena cava [7]. This microvascular network supplies oxygen and nutrients to all cells and organ tissues, as well as transports waste and deoxygenate blood away from those organs. Furthermore, these microvessels networks are not mere conduits for mass transport, but smart systems, which can augment physiological function by initiation of biochemical and biophysical cascades, e.g. vasodilation, vasoconstriction, and wound healing responses. Without the requisite vasculature, engineered tissue constructs are limited by diffusion or single-source fluid channels, and MPS are relegated to very small tissue constructs, often in 2D orientations, with only nutrients to support one or two cell types specific to the organ of interest. Small MPS without fluid networks, similar in size to a single well of a 96-well plate, fail to address the need for dynamic, vascularized tissue constructs with realistic microanatomies and supporting cell types [8]. Additionally, because the nutrients are only supplied through a single inlet and outlet, if at all, the throughput of a single small MPS is severely limited in time to endpoint analysis as the cells proliferate past capacity [9]. Without a vasculature network in the MPS, the complete physiological picture is missing for the organ tissue.

Consequently, engineered tissue constructs require proper vascularization to recapitulate true physiological response. Without control over the fluid dynamics within a system, these phenomena cannot occur. There are two strategies for creating blood vessels in vitro: directed formation and spontaneous formation. Directed formation creates vessels using predefined scaffold geometries [10–16]. Although the directed formation strategy allows for precisely patterned vascular networks with total fluid control [17–21], it is difficult to create small (<100 \mu m in diameter) vessels due to the physical limitations of biofabrication techniques. Additionally, directed formation vessels requires millions of cells and large volumes of media to provide enough biological material to line the inside and surrounding of the vessel structures. During spontaneous formation of vasculature inside MPS, vessels form in a scaffold via angiogenesis, as cells proliferate and branch off to form a more complex vasculature network [22–26]. The limiting factor of a system relying on spontaneous vessel formation is the inability to precisely control fluid movement through formed vessels.

Control of the fluid dynamics is critic for proper development of vascularized microtissues. For example, endothelial cells will polarize along flow direction *in vivo*, which occurs due to shear stress acting on the cell *via* moving blood or lymph. These cells will undergo genetic and molecular changes due to this shear stress, *e.g.* up-regulation of various genes and secreting important angiogenic and barrier function biomarkers [27,28]. Consequently, engineered tissue constructs require proper vascularization to recapitulate true physiological response. Without control over the fluid dynamics within a MPS, these phenomena cannot occur.

Unfortunately, MPS are often one-off creations of a basic functional unit of the organ of interest. Complex MPS designs limit reproducibility and comparability, as fabrication techniques differ immensely across labs or companies. Fortunately, with the help of integrated sensors [29] and functional testing [30], we are moving toward more standardized MPS validation, but often only endpoint analyses determine the functionality or performance of MPS. In essence, from the initial construction of the MPS to the sacrifice of MPS, most are "black boxes" which generate no data on development or function. Sacrificing MPS replicates for quality assurance limits the power and increases the cost of each potential study, and this practice can be detrimental to studies aiming to use allogeneic cell sources. Noninvasively monitoring and controlling MPS is required for future use in preclinical trials [31]. A number of systems have been demonstrated with on-chip monitoring of liquid flow, oxygen [32], and barrier permeability [33].

Herein, we describe a new strategy for monitoring, classifying, and quantifying the progression and ultimate degree of vascular development in engineered microtissues. The non-invasive, nondestructive monitoring and characterization of the microscale fluid network is achieved via in-line sensing of fluid flow rates and correlating these measurements to the hydrodynamic resistance. Integrating a flow sensor as part of the MPS platform and designing the fluidic resistance of the inlet and outlet reservoirs provides a means to quantify the hydrodynamic resistance of the engineered tissue, which is directly proportional to the characteristics of the resident microvessel network. Computational fluid dynamics simulations guided the device design and the development of mathematical models that describe the fluid dynamics. Models with various aspects of vascular angiogenesis demonstrated measurable and quantifiable changes in the fluidic volume of the manifold device. Fig. 1 illustrates the concept of the device and the response to changing fluidic network.

# 2. Materials and methods

# 2.1. Materials

Negative photoresist, SU-8 2100, was obtained from Kayaku Advanced Materials (Westborough, MA). Silicon wafers, 100 mm in diameter, were obtained from University Wafer. Polydimethylsiloxane (PDMS) was obtained from Dow Corning as product Sylgard 184. Sodium dodecyl sulfate (SDS) was purchased from VWR Life Science. The SLI-1000 flow sensor was purchased from Sensirion Inc. Tygon® tubing was obtained from McMaster-Carr. Harvard Apparatus 11 Plus syringe pump was used to drive the fluid in the fluidic networks.

# 2.2. Simulations

COMSOL® Multiphysics (Burlington, MA) was used to perform computational fluid dynamics simulations of the microfluidic manifold device. The device reservoir spaces were modeled as rectangular prisms with dimensions of 2 mm width, 3 mm height, and 26 mm length. The vessels were modeled as cylinders with a diameter of 500 µm and a length of 13 mm. Branched vessels were modeled as 5 mm long cylinders extending from the middle of the original vessels at a 45° angle. The pressure jumper was modeled as a curved cylinder (semi-torus), with a diameter of 1000 µm and a length of 31.4 mm (outer diameter of 10 mm). Device models used in COMSOL® simulations are provided in ESI. The fluid density and viscosity were set at 1000 kg  $\times$  m<sup>-3</sup> and 0.001 Pa  $\cdot$  s, respectively. The inlet was modeled as a standard mass flow rate of 1000  $\mu L \; min^{\text{--}1}$  for all simulations. The outlet was modeled as a pressure being open to the atmosphere, as it feeds to an off-chip reservoir equilibrated with ambient environment. A physics controlled mesh, on "Finer" setting, was applied to the model. Pressure and velocity heat maps were generated, along with cut plots of the pressure profile along the axes of the jumper and vessels. Simulations of anastomosis were carried out using the same parameters as described above except more vessels were added at varying angles connected to the original vessels without connecting to the reservoirs or jumper.

# 2.3. Device Fabrication

The microfluidic manifold devices were fabricated *via* replica molding of PDMS from patterned master molds. The master mold was fabricated *via* photolithography with details of the photomasks and fabrication provided in the ESI (Fig. S3). Briefly, negative photoresist SU-8 2100 was spin-cast on a cleaned and dehydrated silicon wafer at 500 rpm for 8 s, followed by a high-speed spin

for 30 s. For devices with SU-8 thickness of 100 µm, spin speed for 2000 rpm was used; for devices with 200-μm thickness, spin speed was 1100 rpm. After spin casting, the wafers were soft baked on a hot plate at 65 °C and then at 95 °C per manufacturer guidelines. After soft baking, wafers were cooled to room temperature before being UV exposed on MA6 mask aligner under hard contact with a UV filter. After UV exposure, wafers were left on a level surface for 10 min and were then baked at 65  $^{\circ}$ C, then at 95  $^{\circ}$ C, and then cooled to room temperature. The SU-8 was then developed in SU-8 Developer to wash away the unexposed photoresist for approximately 20 min. Developed wafers were rinsed with fresh SU-8 Developer and isopropanol before being dried with nitrogen. Master mold wafers were hard baked at 130 °C for 60 min before replica molding. Channel heights were measured using a KLA-Tencor P-6 profilometer. Each mold was measured in at least 9 locations across the channels. Thicker molds ( $\tilde{3}00-400 \mu m$ ) were made using a 2-step spinning and baking process of thinner (1500 rpm high-speed spin or 150 um) SU-8 layers. Device replicas were cast from the master molds using PDMS at a 10:1 elastomer to curing agent ratio, cured at 60 °C for 90 min, then bonded to a glass slide via oxygen plasma. The two large reservoirs were cut through the entire thickness of the first PDMS layer. A second piece of PDMS encapsulated the entire device with punched ports for the inlet, outlet, and jumper connections. A schematic of the fabricated PDMS devices is provided in the ESI. Harvard Apparatus 11 Plus syringe pump accurately supplied fluid to the device, as verified by the weight of the fluid collected from the outlet. A Sensirion SLI-1000 flow rate sensor was connected in-line to a Tygon® tubing pressure jumper. The thicker molds (300–400 μm) were measured by cutting the device and imaging the cross section (Nikon TE-2000E microscope).

# 2.4. Device operation

Tubing for the inlet, outlet, and two pre-sensor tubing segments were inserted directly into the PDMS devices. The tubing connected to a syringe pump drove fluid to the device. Each device was primed with a 1% solution of SDS in DI water to fill the entire channel and ensure continuity of fluid. The mathematical theory of the parallel branches having the same pressure drop only holds true if the fluid is continuous. DI water with food coloring was used to verify that the fluid was continuous in the device before testing. Two tubing segments connected the flow sensor to the PDMS device. The fluid pumping was then resumed to establish the flow loop within the device and sensor. The total inlet flow for all devices was set to  $1000~\mu L~min^{-1}$ . After allowing the fluid flow to stabilize, flow rate measurements were recorded for a period of 1 min. This ensured an accurate and averaged flow rate measurement for comparison to other devices.

# 3. Results and discussion

# 3.1. Device design

We designed a microfluidic manifold device with branching "vessel" flow by connecting two large reservoirs with small parallel channels, as demonstrated in Fig. 1a. The volume between the manifolds encompasses the fluidic network of the device. An additional pressure jumper with an inline flow meter connects the two manifolds. A pump, connected at the inlet or the outlet, maintains the desired total flow rate through the device. By keeping the dimensions of the reservoirs significantly larger than the channel geometry in the fluidic network, the pressure drop across each manifold is negligible, as compared to the network. Consequently, the pressure drops across each vessel and the jumper are equal. If over time, the fluidic network was to increase in size through

thicker vessels or additional branches, the hydraulic resistance of the network would decrease, leading to an observable decrease in the flow rate through the pressure jumper.

#### 3.2. Mathematical model

Based on Poiseuille's Law, the flow through a rigid cylindrical

$$Q = \Delta P \frac{\pi r^4}{8\mu L} \tag{1}$$

where Q is flow rate,  $\Delta P$  is the pressure difference across the channel, r is the radius of the channel,  $\mu$  is dynamic viscosity, and L is the length of the channel. By substituting the hydraulic resistance,  $R_h$ , fluid flow equation becomes analogous to Ohm's Law:

$$Q = \Delta P \times R_h \tag{2}$$

With the Ohm's Law equivalent in mind, the proposed device is similar to a multimeter in parallel with a resistive network, which measures the voltage across the network. The pressure drop of the fluidic device can then be described in terms of system hydraulic resistance,  $R_s$ , and jumper hydraulic resistance,  $R_i$ ,:

$$\Delta P = Q \left( \frac{1}{R_j} + \frac{1}{R_s} \right)^{-1} \tag{3}$$

If the hydraulic resistance of the fluidic network were to decrease, through the increase in the radii of the channels, r, the decrease in length of channels, l, or formation of additional channels, the corresponding decrease in  $R_S$  can be detected via a decrease in flow rate across the jumper and correlated to the changes in the fluidic network. As such, the proposed fluidic network monitoring system is equivalent to making an electrical measurement across a resistive network, as shown in Fig. 2.

# 3.3. Simulations

Computational fluid dynamics simulations were performed to demonstrate the operating principles of the manifold device and simulate the response of the device to changes in the network. Details of the device geometry are provided in the ESI. Fig. 3a shows the results of finite element analysis for the original model, one with 8 additional branches, and one with 16 additional branches. Large dimensions of the manifolds compared to the branches created a nearly identical pressure drop across all of the main branches and the pressure jumper. Pressure profile across the top most main branch (Fig. 3b) showed a pressure drop of 9.9 Pa between the two manifolds for the original device. The pressure drop across the pressure jumper was 9.9 Pa for the original device as well (Fig. 3c). The addition of 8 more branches to the original device reduced the pressure drop between the two manifolds to 9.5 Pa. As more branches were added (16 branches) the pressure difference between the two manifolds decreased to 9.0 Pa. Under the condition of constant flow rate (see Eq. 3), the observed decrease in the pressure drop is due to the decrease in hydraulic resistance of the network with additional

The pressure drop for the original device with non-interconnected main branches showed a linear pressure drop across the main branches (Fig. 3b). With 8 additional interconnected branches the pressure drop across the main branch was no longer linear due to the new interconnections between branches, as seen in Fig. 3b for *x* position 6.5–13 mm. The number of interconnections between the main branches increased further with 16 branches and the pressure drop across the main branch was not linear across most of its length. Unlike the branches in the device

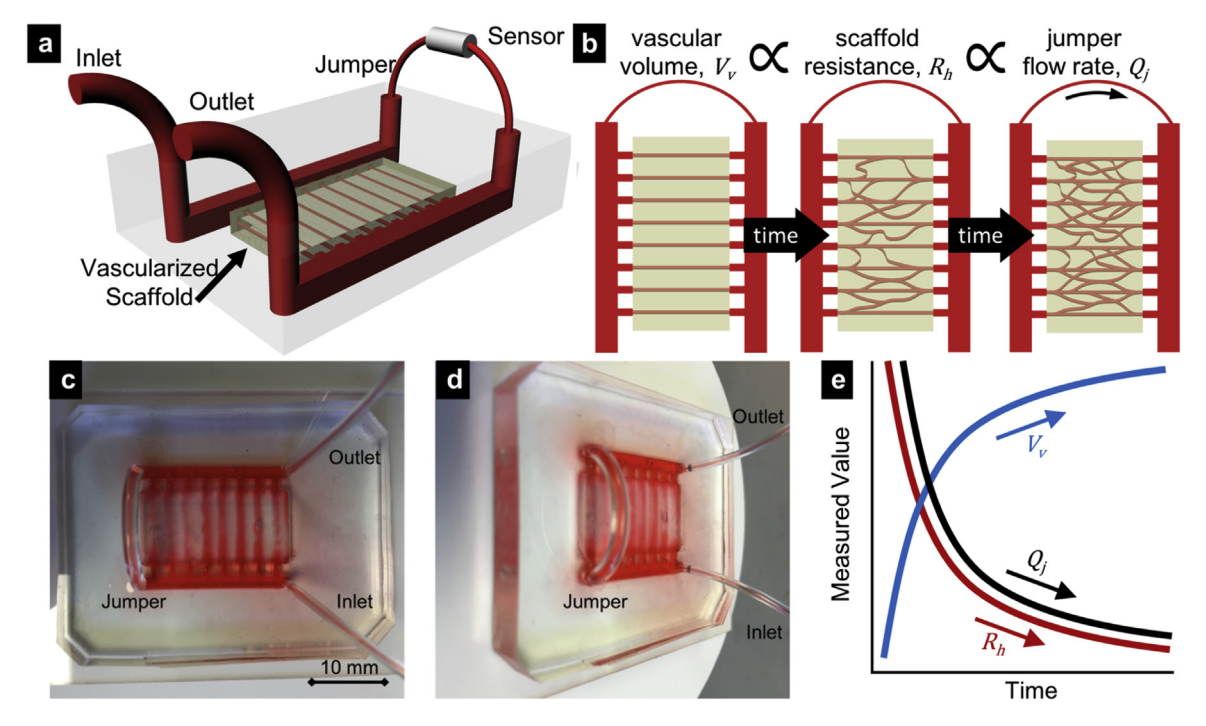
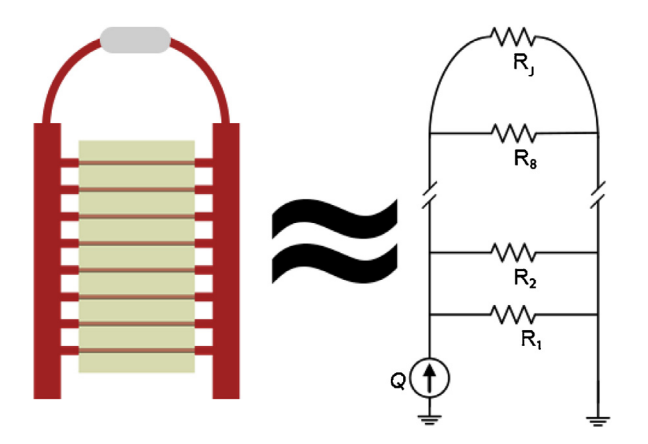


Fig. 1. a) 3D model of the manifold with pressure jumper and inline sensor. b) Schematic representation of how "a living" network might change over time. c, d) images of a prototype manifold device. e) Plot representing the relationship between fluidic volume, scaffold resistance, and jumper flow rate.



**Fig. 2.** Proposed manifold device to monitor a fluidic network and the equivalent circuit model.

network, the pressure jumper maintained a linear pressure drop in all simulated models.

In COMSOL® simulations, it was observed that not all of the new segments contribute to the fluid flow and the hydraulic resistance of the network. The branches without a path to the manifolds (the "dead-end" segments) do not exhibit a pressure gradient or flow and do not contribute to the overall hydraulic resistance. This is an important corollary, as new branches will not contribute to the hydraulic resistance of the network until they bridge into an existing branch or the manifolds.

# 3.4. Experimental devices

We fabricated test devices using soft lithography to investigate the relationship between jumper flow rate and fluidic network changes. Branching devices, similar to the ones used in COMSOL® modeling were fabricated for testing (Fig. 4a), except with rectangular channels, in place of circular channels [34], due to our SU-8 lithography process. Additional device models with channel

splitting without and with the conservation of cross section area were fabricated (Fig. 4b). Furthermore, a third group of masks was designed to mimic a pseudo-randomly generated network with varying degree of branching and splitting (Fig. 4c). In addition, models were evaluated with various SU-8 master mold heights to investigate the effect of expanding fluidic network.

In devices with varying degree of branching, the jumper flow rate decreased with increasing number of interconnected channels, similarly to the COMSOL® results. 16-channel model has the largest number of interconnected branches and the lowest jumper flow rate for similar SU-8 mold height (Fig. 4a). SU-8 mold height has a non-linear effect on hydraulic resistance; therefore, comparisons of the model effects on jumper flow rate should be compared for a narrow range of similar SU-8 mold heights.

Models with varying degree of channel splitting showed a decrease in jumper flow rate, as compared to the original device. The difference between split once and twice models was SU-8 mold height dependent and increased with increasing SU-8 mold height, in contrast to the difference between branching models (Fig. 4a), which decreased with increasing SU-8 mold height.

Pseudo-randomly generated fluidic networks maintain the original design of 8 main branches with the additional branching and interconnections and therefore, hydraulic resistance can only decrease with increasing branching and interconnections. As expected, jumper flow rate decreased in these pseudo-randomly generated networks (Fig. 4c). The difference in the flow rate between the original and pseudo-random models was significant, but differences between the minor and major network models were limited. This suggest that the initial development from the starting vessels exhibits the largest observable change, and as the network development progresses, the identifiable change in flow rate is reduced.

# 3.5. Equivalent circuit model

Demonstrating the effect of fluidic network geometry on flow rate is limited by fabricated SU-8 molds due to compounding vari-

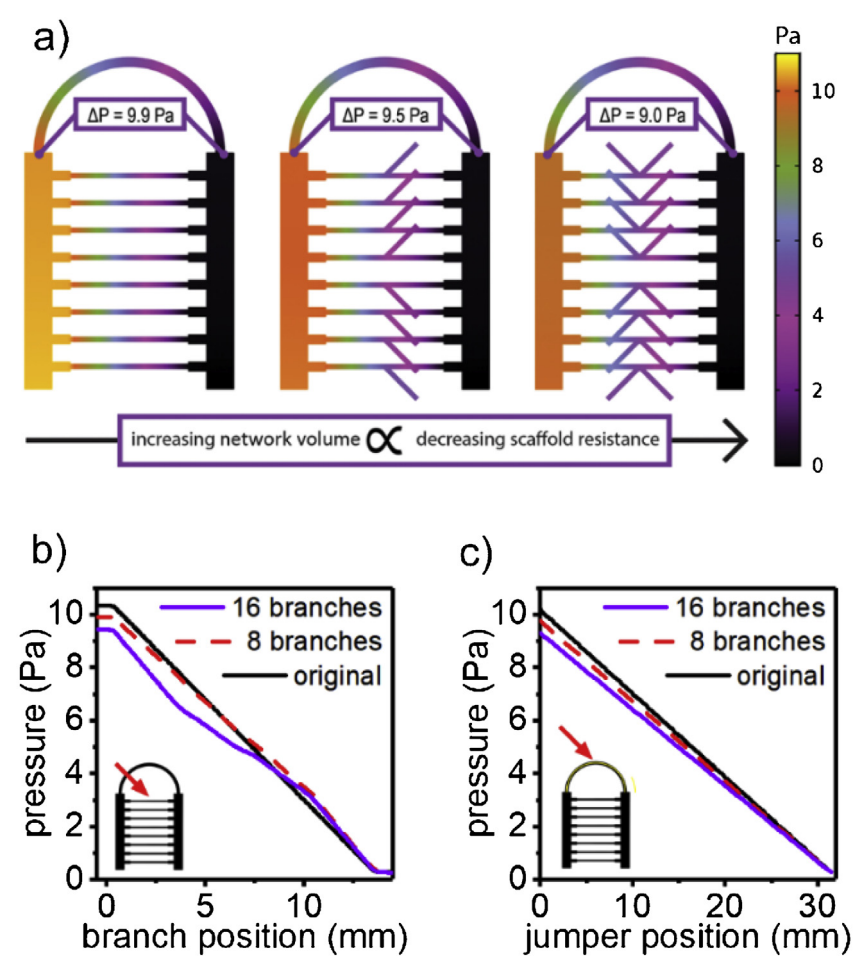


**Fig. 3.** COMSOL® simulation of the proposed manifold device and one with additional 8 or 16 interconnected branches. a) As more branches are added, the network volume increases, leading to a decrease in hydraulic resistance, which results in a decrease in the pressure drop across the scaffold and the jumper. Pressure drop across main branches b) and the pressure jumper c) decreases with increasing network volume.

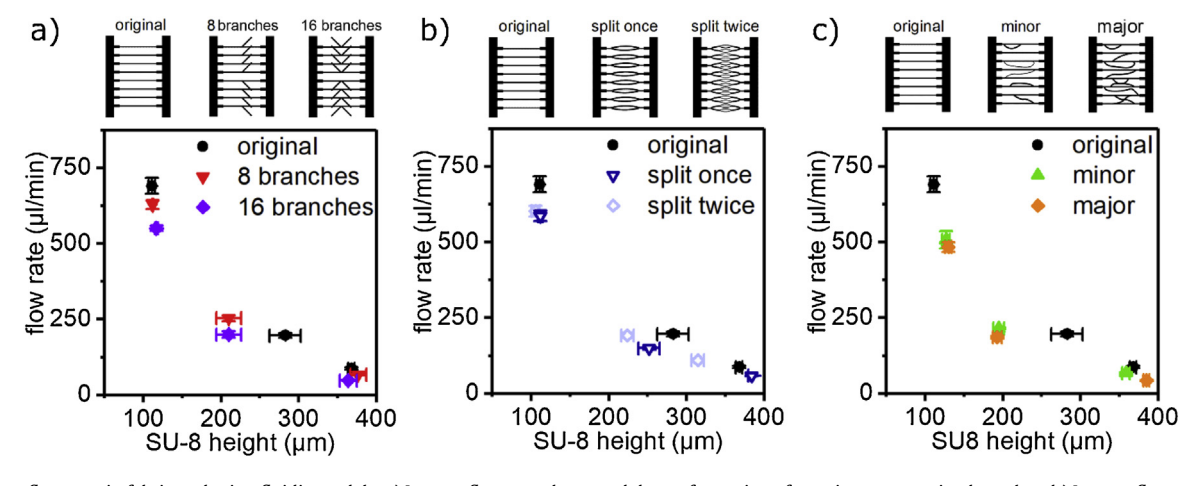


Fig. 4. Jumper flow rate in fabricated microfluidic models. a) Jumper flow rate decreased due to formation of new interconnecting branches. b) Jumper flow rate decreased with increasing splitting of channels. c) Jumper flow rate decreased with increasing fluidic volume in pseudo-random network.

ations in fabrication and the improbability of fabricating every imaginable variant. Finite element analysis (COMSOL) enables accurate simulations of fluid dynamics in 3-D manifold device models, but it is computationally expensive. Electrical circuit analog model for microfluidics is frequently used to solve a complex microfluidic models with close agreement to simulations and experimental results [35]. To examine the flow rate of the pres-

sure jumper attached to different variations of the microscale fluid network, electrical circuit analogs of model devices were created and solved with further details provided in ESI. Current mesh loop analysis was used to solve the system of equations using MATLAB with detailed calculations provided in the ESI.

First, analog equivalent circuit models of the branching designs (Fig. 3a) were calculated and compared to the COMSOL® simula-

**Table 1**Comparison of pressure drop across the pressure jumper using COMSOL® and equivalent circuit models.

Model	$COMSOL^{\$}\DeltaP\left(Pa\right)$	circuit $\Delta P$ (Pa)	error (%)
original	9.9	9.66	- 2.4
8 branches	9.5	9.31	-2.0
16 branches	9.0	8.79	-2.3

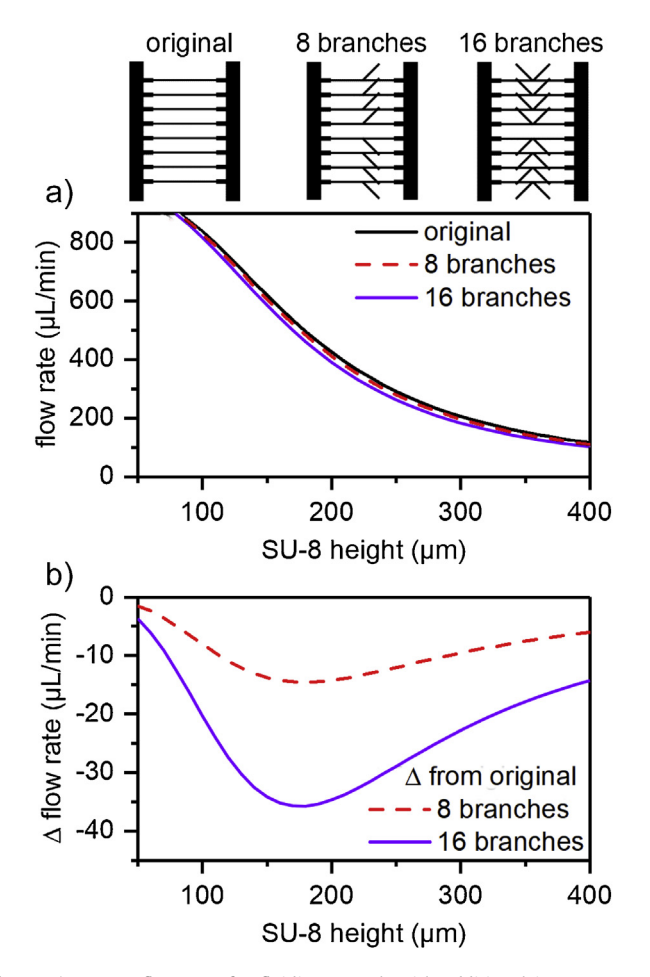


**Fig. 5.** a) Jumper flow rate for fluidic network with additional interconnected branching. b) The flow rate decreases with increasing branching. Response of jumper flow rate with SU-8 height demonstrates the resonance between the jumper and the network.

tions. For these calculations, cylindrical geometry was used with additional details and equations in the ESI. Results of the validation are summarized in Table 1. There is excellent agreement between COMSOL® simulations and the solutions to the equivalent circuit model. The average error of between the models' predictions of the pressure in the jumper is on average -2.2 %.

After the comparison to the COMSOL® simulations, the effects of channel dimensions were characterized by solving the equivalent circuit models for jumper flow rate  $(I_j)$ . In place of the cylindrical channels used for the COMSOL® comparison, a rectangular channel geometry was assumed for this calculation to compare the equivalent circuit models with the fabricated models. The general trends and effects of fluidic network changes on measured flow rate are similar for cylindrical and rectangular vessels. Equations, calculations, and comparison between vessel geometries are provided in the ESI. The effects of microchannel height (or SU-8 mold thickness) and interconnected branching on the jumper flow rate are shown in Fig. 5.

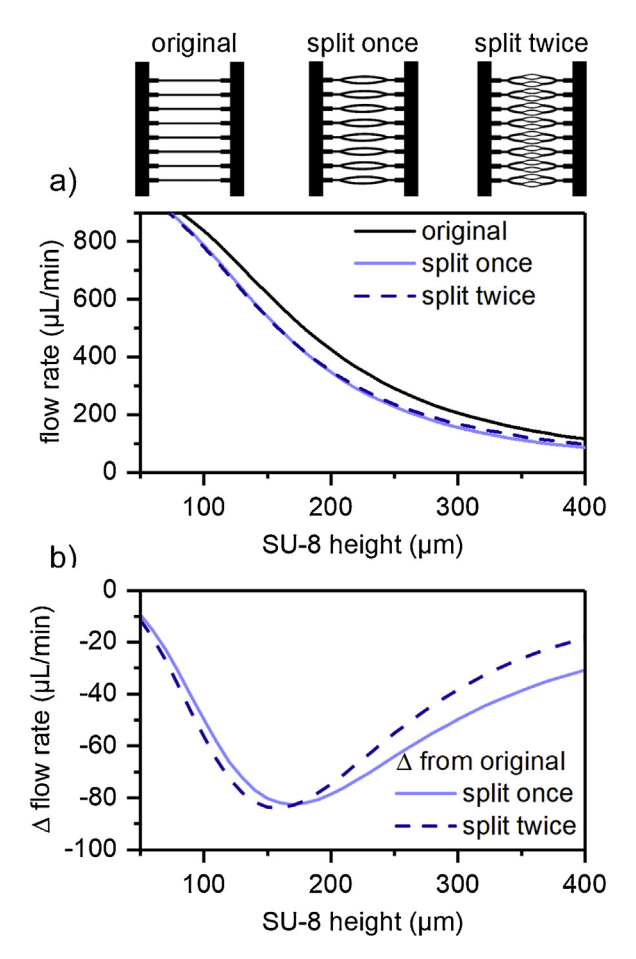


**Fig. 6.** a) Jumper flow rate with varying degree of channel splitting. b) Resonance response of jumper flow rate to changes in fluidic volume. At lower SU-8 height split twice response is dominated by increased fluidic volume and at higher SU-8 height the response is dominated by resistance of narrow channels.

Increasing SU-8 mold height mimics increasing channel cross section, which led to decreasing jumper flow rate for all models. The response of the jumper flow rate to changing network hydraulic resistance is more clearly visualized as the difference between the original and the two branching models in Fig. 5b. Jumper flow rate for branching models was consistently lower than original, with the 16 branches model having the lowest flow rate of the three variants. Increasing the number of interconnected branches decreases the jumper flow rate due to the decrease in the fluidic network resistance, as was observed from resistor network models in Fig. 5. The measured flow rate in the jumper is the result of the resonance between jumper resistance and network resistance, which produces maximum response when two resistances are equal.

In tissue vasculature, aside from branching, living vessels could undergo various splitting, as demonstrated in Fig. 6. The effect of splitting vessels into two equal cross section vessels demonstrates the effect of splitting and angiogenesis with vessels growing out to the original size; this scenario is modelled as split once. In these models, the splitting increased the fluidic volume, decreased the hydrodynamic resistance and increased the flow rate through the fluidic network, as the jumper flow rate decreased, as expected.

In the case of split twice (Fig. 6), the existing channels further split into two channels while maintaining cross-sectional area and the new channel sections have half of the original width. In such ideal case, the fluidic volume does not change, but hydraulic resistance increases. Increase in hydraulic resistance due to small channel width will increase the network resistance and increase the flow rate across the jumper. As seen from Fig. 6b, our model

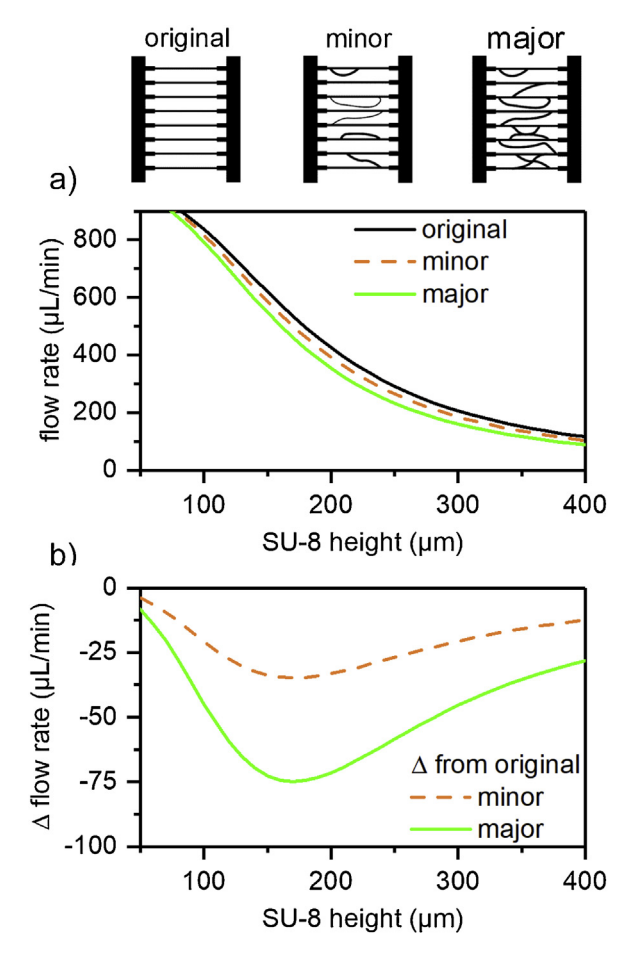


**Fig. 7.** Response of MPS to pseudo-random geometry network. a) Jumper flow rate decreases with decreasing network resistance. b) Degree of network reconstruction is correlated to changes in flow rate.

supports this explanation but deviates from this trend at low SU-8 heights. The non-ideal implementation of splitting and a small increase in the fluidic volume causes this difference between split once and split twice models. At small channel heights, the effect of small channel width is negated by the overall increase in fluidic area and volume. As shown previously, an increase in fluidic area results in lower hydraulic resistance and pressure jumper flow decrease. As SU-8 height increases and approaches the width of the new vessels (250  $\mu m$ ), the hydraulic resistance starts being dominated by the narrow channel width in the split twice model. This phenomenon makes our model sensitive to changes in fluidic geometry, not solely the fluidic volume.

Changes in jumper flow rate were also calculated for models with pseudo-randomly generated fluidic network (Fig. 7). There is a large change in jumper flow rate between the original network and minor network. Upon further, branching and channel growth (major), the jumper flow rate decreases more, as the network resistance decreases further. These changes in jumper flow rate were due to a combination of various branching and splitting geometries and lack clear characteristics to resolve the network geometry.

Fig. 8 summarizes the investigated effects of geometry on fluidic network volume and on the jumper flow rate. Generally, the flow rate decreases with increasing fluidic network volume due to resistance resonance between the network and the jumper. Most notably, the dead-end branches do not contribute to the fluidic volume of the network until they branch into an established channel or the reservoir. In addition, channel splitting initially increases the jumper flow rate. Based on the presented work, it is possible to detect branching and splitting events by their characteristic effect on the jumper flow rate. With additional information on starting geometry and a set of constraints on channel growth, we propose that it will be possible to reconstruct the network geometry through real time monitoring. As is the case, the development of vascular networks is governed by well know scaling laws that dictate the geometric progression of blood vessel formation, [36] and with such constraints, the simple quantification of hydrodynamic resistance can provide metric of vascular development.

In the proposed manifold device, hydraulic resistance of the pressure jumper and sensitivity of the flow meter are critical parameters to optimize for each network. For guidance in system design, the entire system can be reduced to a pressure jumper,  $R_j$ , in parallel with the network,  $R_s$ , and from this the response of the flow meter,  $I_j$ , to the change in network volume can be calculated as

$$\frac{dI_j}{dR_s} = \frac{QR_j}{\left(R_s + R_j\right)^2} \tag{4}$$

where Q is the flow rate of the supply pump, which could be set by the desired shear force in the MPS. From this equation, one is able to select the appropriate jumper resistance,  $R_j$ , to be able to detect network changes,  $dR_s$ , using a flow meter with a specified sensitivity,  $dl_j$ . Depending on the network and the available hardware, the pressure jumper and flow sensor will be changed as fluidic network grows.

Our experimental results follow the same trend as the calculated results, but the observed jumper flow rate is lower than calculated. This difference is attributed to the deviation of the fabricated SU-8 devices from ideal vertical sidewall and exact lateral dimensions. Additional source of error are tubing dimensions; nominal inner diameters were used for calculations, which is not accurate, especially for the tubing compression fitted into the PDMS. Both of these

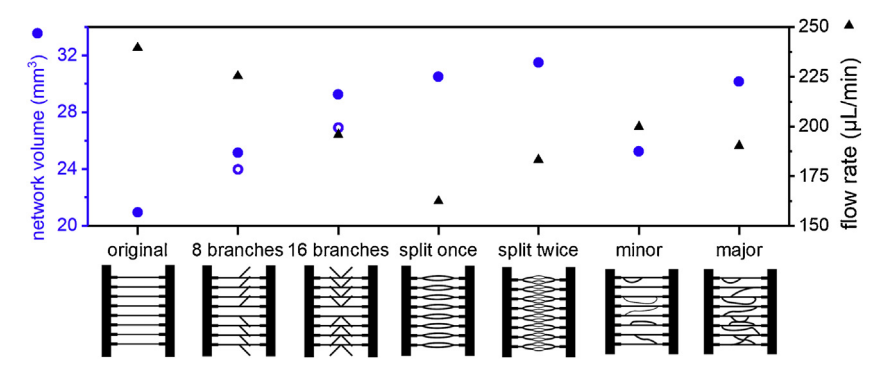


Fig. 8. Calculated effects of geometric network changes on fluidic network volume and jumper flow rate for models with 250 μm mold height. Unconnected branches do not contribute to the pressure gradient in the device and should not contribute to the fluidic network volume, as demonstrated for branching variants.

sources of error will be minimized with real time measurements, where the difference in flow rate over time is of interest.

# 4. Conclusion

In summary, we presented a strategy to quantify the hydrodynamic resistance of a microscale fluid network. We demonstrated this strategy with an instrumented microfluidic device to monitor fluid perfusion through models of vascularized tissue constructs. We developed an equivalent circuit model of the system to rapidly simulate and predict the characteristics of diverse vascularized systems, e.g. different vessel densities, connectivity, and sizes, that are representative of distinct organ systems or functions like angiogenesis and anastomosis. Future work will aim to develop an algorithm to recognize patterns of the hydrodynamic resistance over time as they correlated to the development of vascular networks in the engineered tissue constructs.

Ultimately, we foresee an application of this strategy and platform to investigate the properties of MPS and specifically monitor the development and performance of engineered microvascular networks. For example, there has been myriad reports on the design and fabrication of highly vascularized engineered tissues [37–44], and such engineered tissues would benefit from non-invasive, nondestructive means to monitor the evolution of the microvascular network during development. Furthermore, the proposed platform may also operate as a performance monitor during use by reporting any variations in the steady-state perfusions conditions, providing a means to correct or terminate the operation. The flow rate sensor provides a continuous data stream for the feedback control of flow rates and shear stress in the MPS; moreover, in the future, the use of this platform for the real-time characterization of microvascular network development will enable more reproducible MPS and engineered tissues. Increased reproducibility is the next step in the expanding manufacturing and utility of MPS and engineered tissues for fundamental biological research, drug discovery/screening, toxicological analyses, reducing the use of animal testing, and providing higher quality data for preclinical decision-making.

# **Funding**

The National Science Foundation GrantCCSS-1846911 andAmerican Heart Association Grant18TPA34230031supported this work. This work was performed in part at the Chapel Hill Analytical and Nanofabrication Laboratory, CHANL, a member of the North Carolina Research Triangle Nanotechnology Network, RTNN, which is supported by the National Science Foundation, Grant ECCS-1542015, as part of the National Nanotechnology Coordinated Infrastructure, NNCI. K.R.R. was supported by the National Institutes of Health under award number F31DK118859-02 and by the 2019 Howard Hughes Medical Institute Gilliam Fellowship Award.

# **Author's contributions**

Vladimir A. Pozdin and Patrick D. Erb contributed equally to this paper. **Conceptualization:** Michael Daniele, V.A. Pozdin, and P.D. Erb. **Methodology:** M. Daniele, V.A. Pozdin, and P.D. Erb. **Validation and Investigation:** V.A. Pozdin, P.D. Erb., McKenna Downey, and Kristina R. Rivera. **Data Curation:** M. Daniele, V.A. Pozdin, M. Downey, and K.R. Rivera. **Writing (Original Draft Preparation):** M. Daniele, V.A. Pozdin, P.D. Erb, and K.R. Rivera. **Writing (Review and Editing):** M. Daniele and V.A. Pozdin. **Supervision:** M. Daniele. **Funding Acquisition:** M. Daniele. All authors read and approved the final manuscript.

# Appendix A. Supplementary data

Supplementary material related to this article can be found, in the online version, at doi:https://doi.org/10.1016/j.sna.2021. 112970.

# **Declaration of Competing Interest**

There are no conflicts to declare.

# References

- K. Kaarj, J.Y. Yoon, Methods of delivering mechanical stimuli to organ-on-a-chip, Micromachines (Basel) 10 (2019), http://dx.doi.org/10.3390/ mi10100700.
- [2] P. McGonigle, B. Ruggeri, Animal models of human disease: challenges in enabling translation, Biochem. Pharmacol. 87 (2014) 162–171, http://dx.doi. org/10.1016/j.bcp.2013.08.006.
- [3] B. Zhang, M. Radisic, Organ-on-a-chip devices advance to market, Lab Chip 17 (2017) 2395–2420, http://dx.doi.org/10.1039/c6lc01554a.
- [4] D.G. Rudmann, The Emergence of Microphysiological Systems (Organs-on-chips) as Paradigm-changing Tools for Toxicologic Pathology, Toxicol. Pathol. 47 (2019) 4–10, http://dx.doi.org/10.1177/ 0192633318809065
- [5] H. Lee, M. Chung, N.L. Jeon, Microvasculature: an essential component for organ-on-chip systems, MRS Bull. 39 (2014) 51–59, http://dx.doi.org/10.1557/ mrs.2013.286.
- [6] B.A. Hassell, et al., Human organ chip models recapitulate orthotopic lung cancer growth, therapeutic responses, and tumor dormancy in vitro, Cell Rep. 21 (2017) 508–516, http://dx.doi.org/10.1016/j.celrep.2017.09.043.
- [7] G. Serini, et al., Modeling the early stages of vascular network assembly, EMBO J. 22 (2003) 1771–1779, http://dx.doi.org/10.1093/emboj/cdg176.
- [8] U. Marx, et al., 'Human-on-a-chip' developments: a translational cutting-edge alternative to systemic safety assessment and efficiency evaluation of substances in laboratory animals and man? Altern. Lab. Anim. 40 (2012) 235–257, http://dx.doi.org/10.1177/026119291204000504.
- [9] D. Park, J. Lee, J.J. Chung, Y. Jung, S.H. Kim, Integrating organs-on-chips: multiplexing, scaling, vascularization, and innervation, Trends Biotechnol. (2019), http://dx.doi.org/10.1016/j.tibtech.2019.06.006.
- [10] W. Zhang, et al., Elastomeric free-form blood vessels for interconnecting organs on chip systems, Lab Chip 16 (2016) 1579–1586, http://dx.doi.org/10. 1039/c6lc00001k.
- [11] Y. Zheng, et al., In vitro microvessels for the study of angiogenesis and thrombosis, Proc Natl Acad Sci U S A 109 (2012) 9342–9347, http://dx.doi.org/ 10.1073/pnas.1201240109.
- [12] J.S. Miller, et al., Rapid casting of patterned vascular networks for perfusable engineered three-dimensional tissues, Nat. Mater. 11 (2012) 768–774, http:// dx.doi.org/10.1038/nmat3357.
- [13] S.A. Roberts, K.A. DiVito, F.S. Ligler, A.A. Adams, M.A. Daniele, Microvessel manifold for perfusion and media exchange in three-dimensional cell cultures, Biomicrofluidics 10 (2016) 054109, http://dx.doi.org/10.1063/1. 4963145
- [14] Y.S. Zhang, et al., Bioprinted thrombosis-on-a-chip, Lab Chip 16 (2016) 4097–4105, http://dx.doi.org/10.1039/c6lc00380j.
- [15] M.J. Helmedag, et al., The effects of constant flow bioreactor cultivation and keratinocyte seeding densities on prevascularized organotypic skin grafts based on a fibrin scaffold, Tissue Eng. Part A 21 (2015) 343–352, http://dx.doi. org/10.1089/ten.TEA.2013.0640.
- [16] J.M. Chan, et al., Engineering of in vitro 3D capillary beds by self-directed angiogenic sprouting, PLoS One 7 (2012), http://dx.doi.org/10.1371/journal. pone.0050582, e50582.
- [17] X. Wang, et al., Engineering anastomosis between living capillary networks and endothelial cell-lined microfluidic channels, Lab Chip 16 (2016) 282–290, http://dx.doi.org/10.1039/c5lc01050k.
- [18] J.A. Whisler, M.B. Chen, R.D. Kamm, Control of perfusable microvascular network morphology using a multiculture microfluidic system, Tissue Eng. Part C Methods 20 (2014) 543–552, http://dx.doi.org/10.1089/ten.TEC.2013. 0370
- [19] S. Kim, H. Lee, M. Chung, N.L. Jeon, Engineering of functional, perfusable 3D microvascular networks on a chip, Lab Chip 13 (2013) 1489–1500, http://dx.doi.org/10.1039/c3lc41320a.
- [20] M.R. Zanotelli, et al., Stable engineered vascular networks from human induced pluripotent stem cell-derived endothelial cells cultured in synthetic hydrogels, Acta Biomater. 35 (2016) 32–41, http://dx.doi.org/10.1016/j.actbio. 2016.03.001.
- [21] M.L. Moya, Y.H. Hsu, A.P. Lee, C.C. Hughes, S.C. George, In vitro perfused human capillary networks, Tissue Eng. Part C Methods 19 (2013) 730–737, http://dx.doi.org/10.1089/ten.TEC.2012.0430.
- [22] P. Carmeliet, Mechanisms of angiogenesis and arteriogenesis, Nat. Med. 6 (2000) 389–395, http://dx.doi.org/10.1038/74651.

- [23] H. Stratesteffen, et al., GelMA-collagen blends enable drop-on-demand 3D printablility and promote angiogenesis, Biofabrication 9 (2017) 045002, http://dx.doi.org/10.1088/1758-5090/aa857c.
- [24] S. Weinandy, et al., Biofunctionalized microfiber-assisted formation of intrinsic three-dimensional capillary-like structures, Tissue Eng. Part A 20 (2014) 1858–1869, http://dx.doi.org/10.1089/ten.TEA.2013.0330.
- [25] D.M. Supp, K. Wilson-Landy, S.T. Boyce, Human dermal microvascular endothelial cells form vascular analogs in cultured skin substitutes after grafting to athymic mice, FASEB J. 16 (2002) 797–804, http://dx.doi.org/10. 1096/fj.01-0868com.
- [26] A.F. Black, F. Berthod, N. L'Heureux, L. Germain, F.A. Auger, In vitro reconstruction of a human capillary-like network in a tissue-engineered skin equivalent, FASEB J. 12 (1998) 1331–1340.
- [27] D.C. Chong, Z. Yu, H.E. Brighton, J.E. Bear, V.L. Bautch, Tortuous microvessels contribute to wound healing via sprouting angiogenesis, Arterioscler. Thromb. Vasc. Biol. 37 (2017) 1903–1912, http://dx.doi.org/10.1161/ ATVBAHA.117.309993.
- [28] S. Alimperti, et al., Three-dimensional biomimetic vascular model reveals a RhoA, Rac1, and N-cadherin balance in mural cell-endothelial cell-regulated barrier function, Proc. Natl. Acad. Sci. U. S. A. 114 (2017) 8758–8763, http:// dx.doi.org/10.1073/pnas.1618333114.
- [29] Y.S. Zhang, et al., Multisensor-integrated organs-on-chips platform for automated and continual in situ monitoring of organoid behaviors, Proc. Natl. Acad. Sci. U. S. A. 114 (2017) E2293–E2302, http://dx.doi.org/10.1073/pnas. 1612906114.
- [30] A. van den Berg, C.L. Mummery, R. Passier, A.D. van der Meer, Personalised organs-on-chips: functional testing for precision medicine, Lab Chip 19 (2019) 198–205, http://dx.doi.org/10.1039/c8lc00827b.
- [31] A.T. Young, K.R. Rivera, P.D. Erb, M.A. Daniele, Monitoring of microphysiological systems: integrating sensors and real-time data analysis toward autonomous decision-making, ACS Sens. (2019), http://dx.doi.org/10. 1021/acssensors.8b01549.
- [32] K.R. Rivera, et al., Integrated phosphorescence-based photonic biosensor (iPOB) for monitoring oxygen levels in 3D cell culture systems, Biosens. Bioelectron. 123 (2019) 131–140, http://dx.doi.org/10.1016/j.bios.2018.07. 035

- [33] J.F. Wong, C.A. Simmons, Microfluidic assay for the on-chip electrochemical measurement of cell monolayer permeability, Lab Chip 19 (2019) 1060–1070, http://dx.doi.org/10.1039/c8lc01321g.
- [34] M. Fenech, et al., Microfluidic blood vasculature replicas using backside lithography, Lab Chip 19 (2019) 2096–2106, http://dx.doi.org/10.1039/c9lc00254e
- [35] K.W. Oh, K. Lee, B. Ahn, E.P. Furlani, Design of pressure-driven microfluidic networks using electric circuit analogy, Lab Chip 12 (2012) 515–545, http:// dx.doi.org/10.1039/C2LC20799K.
- [36] Y.L. Huo, G.S. Kassab, Intraspecific scaling laws of vascular trees, J. R. Soc. Interface 9 (2012) 190–200.
- [37] B. Yilmaz, A. Tahmasebifar, E.T. Baran, Bioprinting technologies in tissue engineering, Adv Bioch Eng Biotec 171 (2020) 279–319, http://dx.doi.org/10. 1007/10.2019.108.
- [38] D. Kang, et al., Bioprinting of multiscaled hepatic lobules within a highly vascularized construct, Small 16 (2020), doi:ARTN 1905505 10.1002/smll.201905505.
- [39] A.M. Jorgensen, J.J. Yoo, A. Atala, Solid organ bioprinting: strategies to achieve organ function, Chem. Rev. (2020), http://dx.doi.org/10.1021/acs.chemrev. 0c00145.
- [40] N. Puluca, et al., Bioprinting approaches to engineering vascularized 3D cardiac tissues, Curr. Cardiol. Rep. 21 (2019), http://dx.doi.org/10.1007/s11886-019-1179-8, doi:ARTN 90.
- [41] Z. Galliger, C.D. Vogt, A. Panoskaltsis-Mortari, 3D bioprinting for lungs and hollow organs, Transl. Res. 211 (2019) 19–34, http://dx.doi.org/10.1016/j.trsl. 2010.05.001
- [42] J.Y. Park, J. Jang, H.W. Kang, 3D Bioprinting and its application to organ-on-a-chip, Microelectron. Eng. 200 (2018) 1–11, http://dx.doi.org/10. 1016/j.mee.2018.08.004.
- [43] J. Paek, et al., Microphysiological engineering of self-assembled and perfusable microvascular beds for the production of vascularized three-dimensional human microtissues, ACS Nano 13 (2019) 7627–7643, http://dx.doi.org/10.1021/acsnano.9b00686.
- [44] D.B. Kolesky, K.A. Homan, M.A. Skylar-Scott, J.A. Lewis, Three-dimensional bioprinting of thick vascularized tissues, Proc. Natl. Acad. Sci. U. S. A. 113 (2016) 3179–3184, http://dx.doi.org/10.1073/pnas.1521342113.